



This is a repository copy of *Spatially-controlled occlusion of polymer-stabilized gold nanoparticles within ZnO*.

White Rose Research Online URL for this paper:  
<http://eprints.whiterose.ac.uk/144246/>

Version: Supplemental Material

---

**Article:**

Ning, Y., Fielding, L., Nutter, J. et al. (3 more authors) (2019) Spatially-controlled occlusion of polymer-stabilized gold nanoparticles within ZnO. *Angewandte Chemie*, 131 (13). pp. 4346-4351. ISSN 0044-8249

<https://doi.org/10.1002/ange.201814492>

---

This is the peer reviewed version of the following article: Y. Ning, L. A. Fielding, J. Nutter, A. N. Kulak, F. C. Meldrum, S. P. Armes, *Angew. Chem.* 2019, 131, 4346, which has been published in final form at <https://doi.org/10.1002/ange.201814492>. This article may be used for non-commercial purposes in accordance with Wiley Terms and Conditions for Use of Self-Archived Versions.

**Reuse**

Items deposited in White Rose Research Online are protected by copyright, with all rights reserved unless indicated otherwise. They may be downloaded and/or printed for private study, or other acts as permitted by national copyright laws. The publisher or other rights holders may allow further reproduction and re-use of the full text version. This is indicated by the licence information on the White Rose Research Online record for the item.

**Takedown**

If you consider content in White Rose Research Online to be in breach of UK law, please notify us by emailing [eprints@whiterose.ac.uk](mailto:eprints@whiterose.ac.uk) including the URL of the record and the reason for the withdrawal request.



[eprints@whiterose.ac.uk](mailto:eprints@whiterose.ac.uk)  
<https://eprints.whiterose.ac.uk/>

Supporting Information  
©Wiley-VCH 2016  
69451 Weinheim, Germany

## Spatially-Controlled Occlusion of Polymer-Stabilized Gold Nanoparticles within ZnO

Yin Ning,<sup>\*[a]</sup> Lee A. Fielding,<sup>[b]</sup> John Nutter,<sup>[c]</sup> Alexander N. Kulak,<sup>[d]</sup> Fiona C. Meldrum,<sup>[d]</sup> and Steven P. Armes<sup>\*[a]</sup>

### Table of Contents

1. Experimental section .....	2
1.1. Chemicals .....	2
1.2. Synthesis of poly(glycerol monomethacrylate) <sub>70</sub> [G <sub>70</sub> ] homopolymer .....	2
1.3. Synthesis of poly(glycerol monomethacrylate) <sub>70</sub> -stabilized gold nanoparticles (G <sub>70</sub> -AuNPs).....	2
1.4. Synthesis of G <sub>70</sub> -Au/ZnO nanocomposite crystal .....	3
1.5. Photocatalytic degradation of RhB using UV irradiation .....	3
2. Characterization .....	4
2.1. <sup>1</sup> H NMR spectroscopy .....	4
2.2. Gel permeation chromatography (GPC) .....	4
2.3. Dynamic light scattering (DLS) .....	4
2.4. Transmission electron microscopy (TEM) .....	4
2.5. Scanning electron microscopy (SEM).....	5
2.6. X-ray photoelectron spectroscopy (XPS).....	5
2.7. Other measurements .....	5
3. Calculation of surface density of G <sub>70</sub> homopolymer chains on AuNPs .....	7
4. Occlusion mechanism .....	8
5. Synthesis and Characterization of G <sub>70</sub> -AuNPs.....	9
6. Scheme .....	10
7. Figures .....	11

DOI: 10.1002/anie.2016XXXXX

## 1. Experimental section

### 1.1. Chemicals

Glycerol monomethacrylate (GMA; 99.8%) was donated by GEO Specialty Chemicals (Hythe, UK) and used without further purification. 4-Cyano-4 (phenylcarbonothioylthio)pentanoic acid (CPCP), 2-cyano-2-propyl benzodithioate (CPB), 2,2'-azobis(isobutylnitrile) (AIBN) 4,4'-azobis(4-cyanovaleric acid) (ACVA), zinc nitrate hexahydrate, hexamethylenetetramine (HMTA), rhodamine B (RhB), sodium citrate tribasic dihydrate, sodium borohydride and gold(III) chloride trihydrate ( $\text{HAuCl}_4 \cdot 3\text{H}_2\text{O}$ ) were all purchased from Sigma-Aldrich (UK) and used as received. Deionized water was obtained from an Elgastat Option 3A water purification unit.

### 1.2. Synthesis of poly(glycerol monomethacrylate)<sub>70</sub> [G<sub>70</sub>] homopolymer

To a round-bottomed flask containing CPCP RAFT agent (0.96 g, 3.43 mmol), GMA monomer (38.44 g, 0.24 mol) and anhydrous ethanol (59.40 g, 1.28 mol) was added to afford a target degree of polymerization (DP) of 70. ACVA initiator (0.19 g, 0.69 mmol, CTA/ACVA molar ratio = 5.0) was then added to this pink solution, which was sparged with  $\text{N}_2$  for 20 min before immersing the sealed flask into an oil bath set at 70 °C. After 2.5 h, the polymerization was quenched by immersing the flask in an ice bath and exposing its contents to air. The polymerization solution was then precipitated into a ten-fold excess of dichloromethane and washed three times with this solvent before being placed under high vacuum for three days at 40 °C.  $^1\text{H}$  NMR analysis indicated a mean DP of 70. Taking into account the target DP of 70 and the conversion of 85 %, this suggests a CTA efficiency of 85 %. DMF GPC analysis (vs. a series of near-monodisperse poly(methyl methacrylate) calibration standards) indicated  $M_n$  and  $M_w/M_n$  values of 17,000  $\text{g mol}^{-1}$  and 1.10, respectively.

### 1.3. Synthesis of poly(glycerol monomethacrylate)<sub>70</sub>-stabilized gold nanoparticles (G<sub>70</sub>-AuNPs)

The synthesis of gold nanoparticles has previously been reported elsewhere<sup>[1]</sup>. In the present study, 480 mL deionized water was charged into a 1000 mL beaker and then 5.0 mL of 10  $\text{g dm}^{-3}$  gold(III) chloride trihydrate was added and stirred for 5 minutes. Thereafter, an aqueous solution of sodium citrate (10 mL, 38.8 mM) was added and stirred for another 5 min before rapid addition of an aqueous solution of sodium borohydride (5.0 mL, 0.075 % w/w), containing sodium citrate tribasic dehydrate

(57 mg, 38.8 mM). G<sub>70</sub> homopolymer (100 mg) was dissolved in 10 mL deionized water and added to the gold sol. Excess G<sub>70</sub> homopolymer and sodium citrate were removed by centrifugation, followed by dialysis against deionized water for 7 days, using dialysis tubing with a molecular weight cut-off of 50 kD.

For the 14 nm gold nanoparticles, 500 mL deionized water was mixed with 30.0 mL 1 % w/w sodium citrate solution in a 1000 mL beaker and boiled for 5 min, followed by the rapid addition of 5.0 mL of a 10 g dm<sup>-3</sup> aqueous solution of gold(III) chloride trihydrate. The reaction was allowed to proceed for 15 min. 100 mg G<sub>70</sub> homopolymer dissolved in 10 mL water was then added and the resulting G<sub>70</sub>-modified gold nanoparticles were purified by multiple centrifugation-redispersion cycles, with successive supernatants being replaced with deionized water.

#### 1.4. Synthesis of G<sub>70</sub>-Au/ZnO nanocomposite crystal

Aqueous G<sub>70</sub>-AuNP dispersions (0.50 g dm<sup>-3</sup>, 2.0 – 30.0 mL) were added to a two-necked flask containing 96.0 – 68.0 ml of an aqueous solution of zinc nitrate hexahydrate (0.446 g, 1.50 mmol) to give a total volume of 98.0 mL. This flask was connected to a condenser and transferred to a preheated oil bath set at 90 °C and the reaction mixture was magnetically stirred to achieve thermal equilibrium (typically 30 min). ZnO formation was commenced on slow addition of 2.0 mL of an aqueous solution of HMTA (0.210 g, 1.50 mmol). The reaction was quenched after 90 minutes by cooling in an ice-water bath. The precipitate was isolated by centrifugation and washed several times using water or ethanol, followed by drying under vacuum at 40 °C. For surface-confined G<sub>70</sub>-Au NP occlusion, G<sub>70</sub>-AuNPs were added to the same reaction solution after 30 min, rather than at the beginning of the reaction.

#### 1.5. Photocatalytic degradation of RhB using UV irradiation

G<sub>70</sub>-Au/ZnO nanocomposites (10 mg) were dispersed in deionized water (18.0 mL) with the aid of an ultrasonic bath for 10 minutes. 2.0 mL of a 1.0 × 10<sup>-4</sup> M RhB stock solution was added and continuously stirred in the dark for 30 min before irradiation using a UV lamp (6 W, peak emission = 254 nm). Aliquots were extracted at various times and centrifuged prior to recording the visible absorption spectrum of the supernatant solution. The photodegradation of the RhB dye was monitored via gradual reduction in its absorption maximum at 553 nm. Photocatalysis experiment was conducted at pH 7 under room temperature (20 °C) and repeated in triplicate.

## 2. Characterization

### 2.1. $^1\text{H}$ NMR spectroscopy

$^1\text{H}$  NMR spectra were recorded using a Bruker Avance 400 spectrometer operating at 400 MHz using  $\text{CD}_3\text{OD}$  as the solvent.

### 2.2. Gel permeation chromatography (GPC)

The DMF GPC instrument comprised two Polymer Laboratories PL gel 5 mm Mixed C columns, one PL polar gel 5 mm guard column connected in series to a Varian 390-LC multi-detector suite (refractive index detector only), a Varian 290-LC pump injection module and was operated at 60 °C. The GPC eluent was HPLC grade DMF containing 10 mM LiBr and was filtered prior to use. The flow rate used was 1.0 mL  $\text{min}^{-1}$  and DMSO was used as a flow-rate marker. Calibration was conducted using a series of ten near-monodisperse poly(methyl methacrylate) standards ( $M_n = 6.25 \times 10^2 - 6.18 \times 10^5 \text{ g mol}^{-1}$ ,  $K = 2.094 \times 10^{-3}$ ,  $\alpha = 0.642$ ).

### 2.3. Dynamic light scattering (DLS)

DLS measurements were conducted using a Malvern Zetasizer NanoZS instrument by detecting back-scattered light at an angle of 173°. The concentration of aqueous dispersions of various gold nanoparticles with or without 15 mM zinc ions were fixed at 0.05 g  $\text{dm}^{-3}$ .

### 2.4. Transmission electron microscopy (TEM)

TEM specimens of gold nanoparticles or  $G_{70}\text{-Au/ZnO}$  nanocomposites were prepared by adsorbing the samples onto carbon film coated palladium-copper grids, which were treated with a plasma glow discharge for about 30 seconds to create a hydrophilic surface prior to addition of the aqueous sample dispersion (5  $\mu\text{L}$ ). Excess solvent was removed via blotting and the grid was carefully dried under vacuum. To examine internal structures, the  $G_{70}\text{-Au/ZnO}$  nanocomposites were embedded in Araldite resin mixture and cured at 60 °C for 48-72 h. Ultrathin sections, approximately 85 nm in thickness, were cut using a Leica UC 6 ultramicrotomy equipped with a Diatome diamond knife onto 200 mesh copper grids. TEM images were performed using either a FEI Tecnai G2 Spirit instrument (120 kV) or a

high resolution TEM instrument (either Philips FEG-CM200 or JEOL JEM-F200) operating at an accelerating voltage of 200 kV. Elemental mapping images were obtained using the JEOL JEM-F200 instrument, which was equipped with dual SDD for EDS analysis.

## 2.5. Scanning electron microscopy (SEM)

The nanocomposite morphologies were investigated using scanning electron microscopy (either a FEI Nova NanoSEM 450 or FEI Inspect F). The specimens were prepared by dropping G<sub>70</sub>-Au/ZnO aqueous dispersion onto a cleaned glass slide and dried at room temperature. All the samples were iridium-coated before imaging.

## 2.6. X-ray photoelectron spectroscopy (XPS)

XPS samples were prepared by adding a drop of nanocomposite aqueous dispersion onto clean indium foil and left overnight at room temperature. The powder samples were directly pressed on a clean indium foil. The instrument used to collect the XPS data was a Kratos Axis Ultra DLD equipped with a monochromatic Al X-ray radiation at 6.0 mA and 15 kV at a typical base pressure of 10<sup>-8</sup> Torr. The step size was 0.5 eV for the survey spectra (pass energy = 160 eV) and 0.05 eV for the high resolution spectra (pass energy = 20 eV). The raw data was corrected by a transmission function characteristic of the instrument, determined using software from the National Physical Laboratory. The adjusted data was then quantified using the theoretically derived Scofield relative sensitivity factors.

## 2.7. Other measurements

FT-IR spectra were recorded on KBr pellets using a Nicolet 7199 FT-IR spectrometer. Thermogravimetric analysis (TGA) was conducted using a Perkin-Elmer Pyris 1 TGA instrument under air atmosphere from 20 °C to 900 °C at a heating rate of 15 °C min<sup>-1</sup>. The elemental analysis was conducted using a Perkin Elmer 2400 Series II CHNS/O Elemental Analyser. Powder X-ray diffraction (XRD) measurements were made using a Bruker D2 Phaser Desktop X-ray diffractometer equipped with Ni-filtered Cu K $\alpha$  radiation ( $\lambda = 1.542 \text{ \AA}$ ) operating at an accelerating voltage and emission current of 30 kV and 10 mA, respectively. The Au content of G<sub>70</sub>-Au/ZnO nanocomposite particles was determined by a Hewlett-Packard 4500 inductively-coupled plasma mass spectrometry (ICP-MS,

Hewlett-Packard, Yokogawa Corporation, Japan). UV-visible spectra were recorded at 20 °C for the nanocomposite aqueous dispersion using a Perkin-Elmer Lambda 25 instrument operating between 200 and 800 nm. Specific surface areas were determined via BET surface area analysis using N<sub>2</sub> as an adsorbate at 77 K. The densities of the G<sub>70</sub>-Au and G<sub>70</sub>-Au/ZnO nanocomposites were determined by helium pycnometry at 20 °C (Micrometrics AccuPyc 1330 helium pycnometer). The number-average mean diameter of the Au nanoparticles was determined by analyzing TEM images (more than 200 AuNPs) using ImageJ software.

### 3. Calculation of surface density of G<sub>70</sub> homopolymer chains on AuNPs

Based on thermogravimetric analysis data, the weight percentage of G<sub>70</sub> homopolymer (W<sub>p</sub>) can be obtained and the weight percentage of the Au cores is readily calculated by difference (see below).

Assuming the mass of G<sub>70</sub>-Au is m, then the mass of G<sub>70</sub> is given by m × W<sub>p</sub>, and the mass of Au is m × (100 - W<sub>p</sub>).

Hence the number of G<sub>70</sub> polymer chains =  $\frac{mW_p}{M_p} N_A$ , where M<sub>p</sub> is the molecular weight of G<sub>70</sub>.

The number of Au nanoparticles =  $\frac{m(100-W_p)}{\frac{4}{3}\pi\rho r^3}$

Total surface area of Au nanoparticles =  $\frac{m(100-W_p)}{\frac{4}{3}\pi\rho r^3} \times 4\pi r^2$

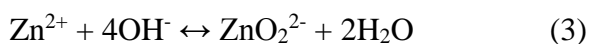
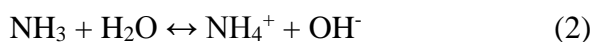
Thus the surface density of G<sub>70</sub> homopolymer chains =  $\left(\frac{W_p}{100-W_p}\right) \times \frac{r\rho N_A}{3M_p} = \left(\frac{40}{100-40}\right) \times$

$$\frac{2.4 \text{ nm} \times 19.3 \text{ g cm}^{-3} \times 6.02 \times 10^{23} \text{ mol}^{-1}}{3 \times 11491 \text{ g mol}^{-1}} = 0.54 \text{ chains nm}^{-2}$$

#### 4. Occlusion mechanism

It is well-known that hexagonal ZnO crystals possess polar (0001) and (000 $\bar{1}$ ) planes, with the former being rich in zinc atoms while the latter is rich in oxygen atoms.<sup>[2]</sup> The relative growth velocity,  $V$ , of each plane follows the order  $V_{[0001]} > V_{[10\bar{1}0]} > V_{[000\bar{1}]}$ . This explains why elongated rod-like ZnO crystals are formed, as shown in Figure 1a. In this study, HMTA is used to generate hydroxide anions via a hydrolysis reaction that produces formaldehyde and ammonia (see reaction scheme shown below).<sup>[3]</sup>

The four main reactions involved in the formation of ZnO crystals are as follows:



In the early stages of ZnO crystallization, anionic  $\text{ZnO}_2^{2-}$  units (the ZnO growth unit under weakly acidic conditions) are preferentially absorbed onto cationic (0001) faces.<sup>[3b]</sup> Meanwhile, HMTA hydrolyzes and forms the cationic (fully protonated)  $(\text{CH}_2)_6\text{N}_4\text{-}4\text{H}^+$  complex in aqueous solution,<sup>[4]</sup> which interacts with the (000 $\bar{1}$ ) face via coulombic interaction.<sup>[3b]</sup> Moreover, this cationic complex also interacts with the  $\text{ZnO}_2^{2-}$  precursor species.<sup>[3]</sup> This leads to the formation of ZnO crystals on the (000 $\bar{1}$ ) surface. Thus, a twinned structure with a common basal plane and 180° reversed polarity is gradually formed via preferential growth in two opposing directions.<sup>[3]</sup>

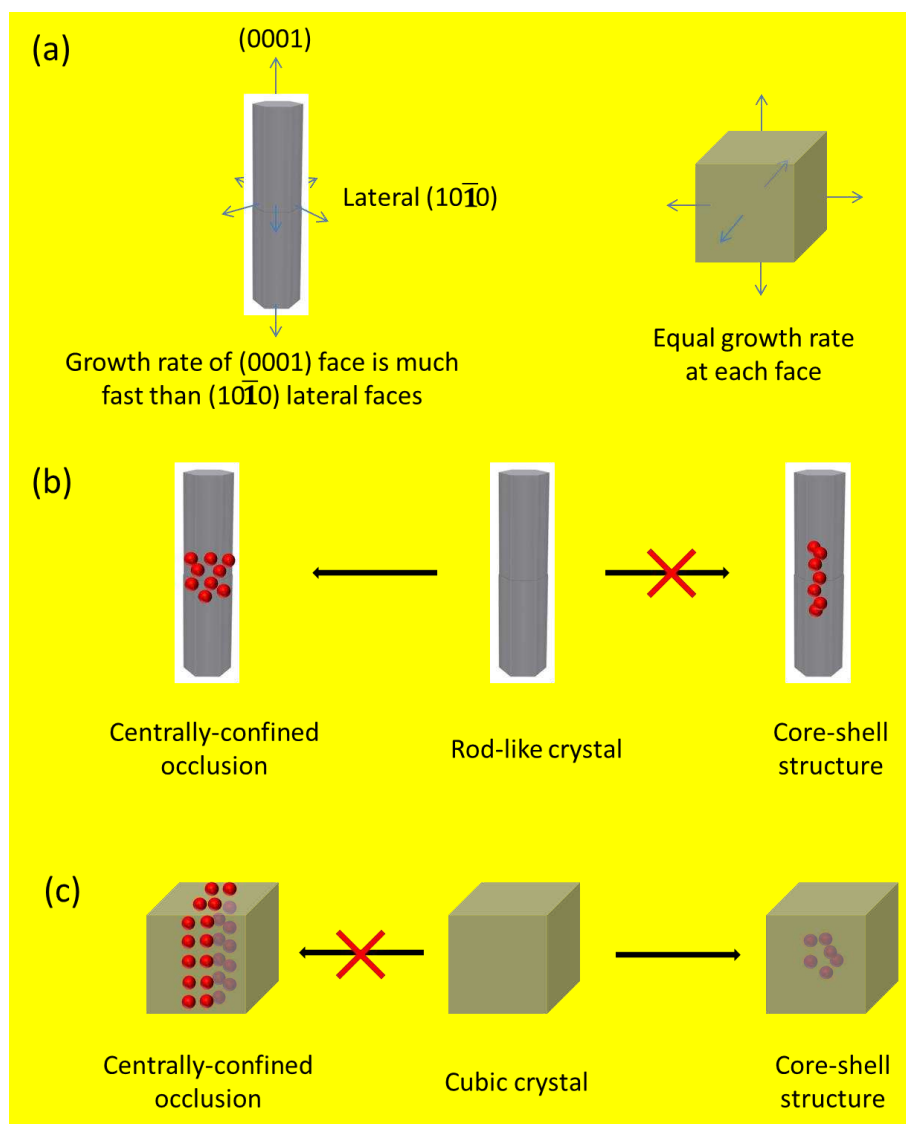
## 5. Synthesis and Characterization of G<sub>70</sub>-AuNPs.

Poly(glycerol monomethacrylate)<sub>70</sub> (see Figure S1a) was synthesized via reversible addition-fragmentation chain transfer (RAFT) polymerization in ethanol using 4-cyano-4-(phenylcarbonothioylthio)pentanoic acid (CPCP) and 4,4'-azobis(4-cyanovaleric acid) as RAFT chain transfer agent and initiator, respectively. This water-soluble G<sub>70</sub> homopolymer contains dithiobenzoate and carboxylic acid end-groups and possesses a narrow molecular weight distribution ( $M_n = 17\,000\text{ g mol}^{-1}$ ,  $M_w/M_n = 1.10$ ), as confirmed by gel permeation chromatography (GPC, see Figure S1b). An aqueous dispersion of AuNPs was prepared as described elsewhere.<sup>[1]</sup> G<sub>70</sub>-AuNPs were prepared via chemisorption conducted in aqueous solution; the dithiobenzoate terminal group on the G<sub>70</sub> chains is known to bind strongly to gold surfaces.<sup>[5]</sup> As shown in Figures S1c and S1d, the as-synthesized G<sub>70</sub>-AuNPs had a mean TEM diameter of  $4.8 \pm 0.9\text{ nm}$ . It is well-known that the surface plasmon band of AuNPs of a given size is sensitive to their surface modification.<sup>[6]</sup> Indeed, the surface plasmon band was red-shifted by 4 nm after surface-grafting the G<sub>70</sub> chains (see inset in Figure S1e). This chemical modification led to a subtle change in color from pink to purple for the AuNP dispersion (see Figure S2). According to dynamic light scattering (DLS, see Figure S3) studies, the mean hydrodynamic diameters of the citrate-stabilized AuNPs and G<sub>70</sub>-AuNPs were  $6.4 \pm 1.6\text{ nm}$  and  $11.5 \pm 2.8\text{ nm}$ , respectively. This difference indicates a G<sub>70</sub> stabilizer layer thickness of  $\sim 2.5\text{ nm}$ , which is consistent with recent small-angle X-ray scattering studies.<sup>[7]</sup> Thermogravimetric analyses (TGA, see Figure S4) indicated that the G<sub>70</sub> stabilizer comprised approximately 40% by mass of the G<sub>70</sub>-AuNPs. This composition was corroborated by carbon microanalyses, which indicated a G<sub>70</sub> content of  $\sim 41\%$ .

The original citrate-stabilized AuNPs aggregate immediately in the presence of zinc ions (see Figures S2 and S3). This salt-induced coagulation is corroborated by the disappearance of the surface plasmon absorbance (see Figure S1e) and the observation of  $\sim 700\text{ nm}$  aggregates by DLS (see Figure S3). In contrast, the surface plasmon band observed for G<sub>70</sub>-AuNPs remains unchanged in the presence of zinc ions (Figure S1e). More specifically, G<sub>70</sub>-AuNPs retain their colloidal stability in the presence of 15

mM  $\text{Zn}(\text{NO}_3)_2$ , which is an essential prerequisite for their subsequent efficient occlusion within ZnO crystals.

## 6. Scheme



**Scheme S1.** (a) Schematic cartoons illustrating the two different growth rates for the eight faces of a rod-like crystal and the identical growth rates for the six faces of a cubic crystal; (b) core-shell structures cannot be obtained for rod-like crystals but centrally-confined occlusion can be achieved; (c) if secondary nucleation is avoided, then a core-shell structure is likely but centrally-confined occlusion is not possible for a cubic host crystal.

## 7. Figures

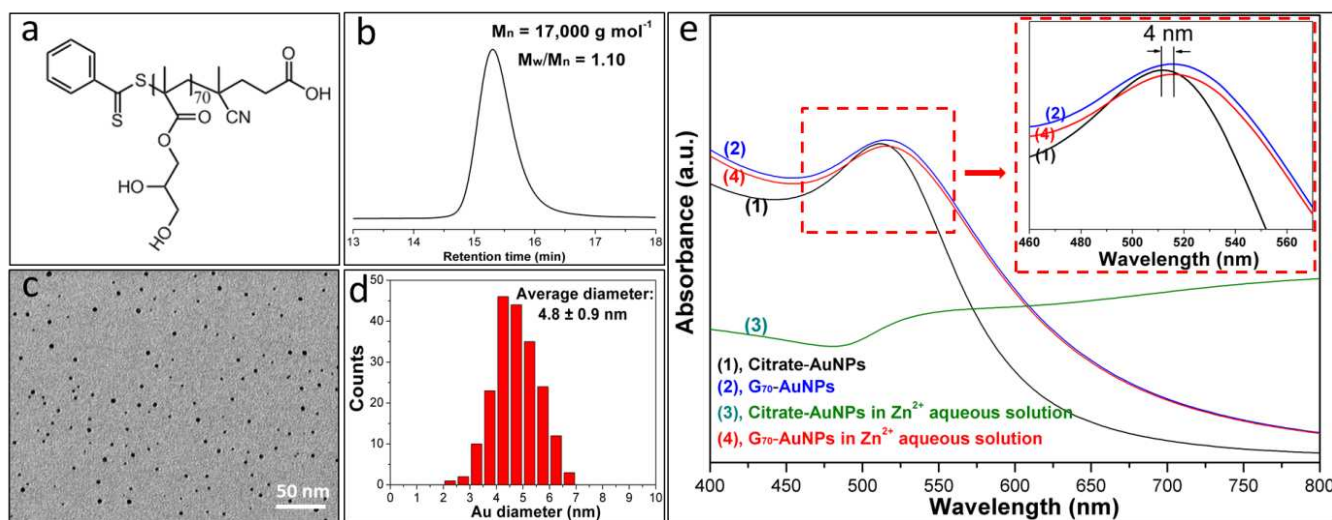


**Figure S1.** Characterization of poly(glycerol monomethacrylate)<sub>70</sub> (G<sub>70</sub>) and G<sub>70</sub>-stabilized AuNPs. (a) Chemical structure of the G<sub>70</sub> polymer; (b) GPC data obtained for G<sub>70</sub> using a series of poly(methyl methacrylate) calibration standards; (c) representative TEM image obtained for G<sub>70</sub>-AuNPs; (d) particle size distribution determined for G<sub>70</sub>-AuNPs from TEM image analysis; (e) Visible absorption spectra recorded for as-synthesized citrate-AuNPs or G<sub>70</sub>-AuNPs in either water or an aqueous solution of 15 mM Zn(NO<sub>3</sub>)<sub>2</sub>. The inset shows that the surface plasmon band for G<sub>70</sub>-AuNPs is red-shifted by 4 nm compared to citrate-AuNPs. Notably, there is no further change in the presence of 15 mM zinc ions, indicating good colloidal stability for the G<sub>70</sub>-AuNPs under these conditions.

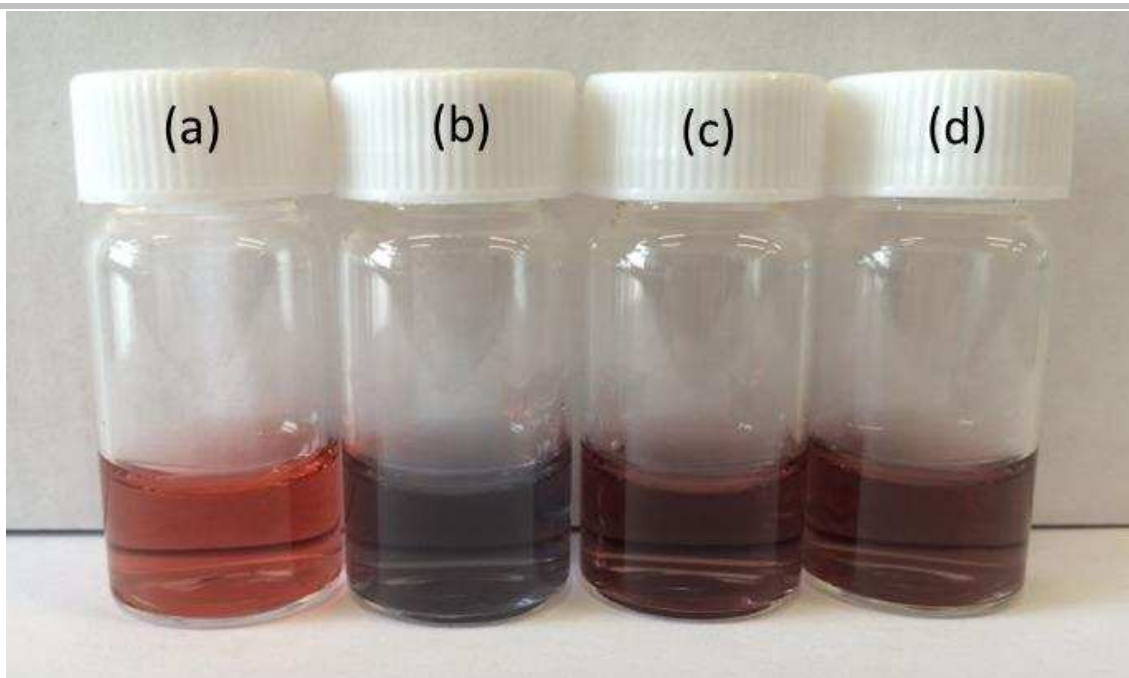


**Figure S2.** Optical photograph of aqueous dispersions of (a) citrate-stabilized AuNPs (gold nanoparticles prepared using sodium citrate); (b) citrate-stabilized AuNPs in the presence of 15 mM zinc ions; (c) G<sub>70</sub>-AuNPs; (d) G<sub>70</sub>-AuNPs in the presence of 15 mM zinc ions. Note: the color of citrate-stabilized AuNPs aqueous solution immediately changed from pink to grey once upon the addition of zinc ions derive from zinc nitrate hexahydrate. This is due to the aggregation of the gold nanoparticle caused by the presence of zinc ions. The aggregation was confirmed by DLS measurements (see **Figure S3**). It is emphasized that there is no discernible colour change between (c) and (d), indicating excellent colloidal stability for the G<sub>70</sub>-AuNPs even in the presence of zinc ions.

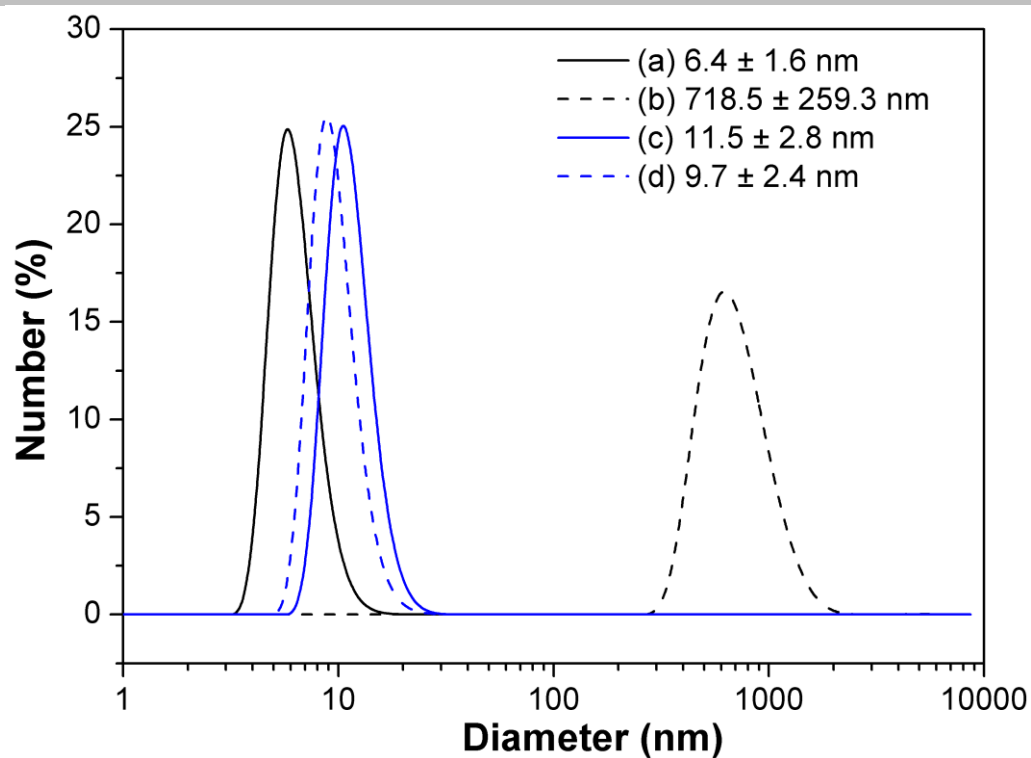


**Figure S3.** Mean hydrodynamic number-average diameter obtained for (a) citrate-stabilized AuNPs in aqueous solution, (b) citrate-stabilized AuNPs in aqueous solution containing 15 mM  $\text{Zn}(\text{NO}_3)_2$ , (c)  $\text{G}_{70}$ -AuNPs in aqueous solution and (d)  $\text{G}_{70}$ -AuNPs in aqueous solution containing 15 mM  $\text{Zn}(\text{NO}_3)_2$ .

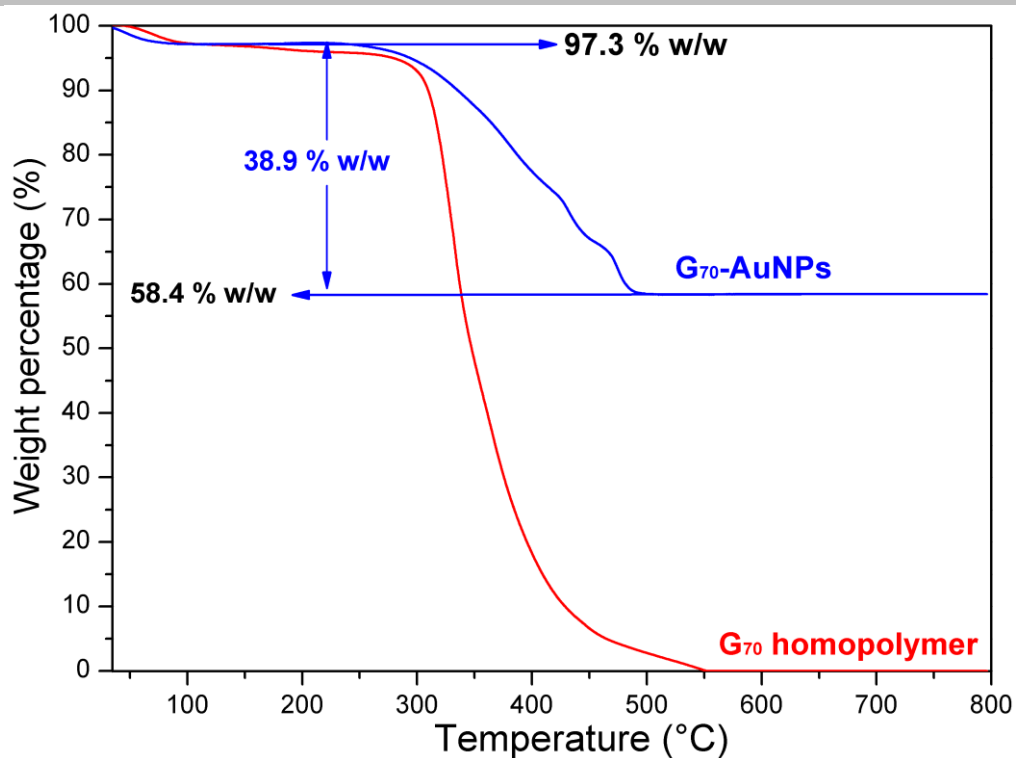


**Figure S4.** Thermogravimetric analysis (TGA) of G<sub>70</sub> homopolymer (red) and G<sub>70</sub>-AuNPs (blue). As expected, G<sub>70</sub> homopolymer is pyrolysed completely above 550 °C. Given the presence of 2.7 % w/w water in the G<sub>70</sub>-AuNPs, the G<sub>70</sub> content of G<sub>70</sub>-AuNPs can be calculated to be 40.0 % w/w.

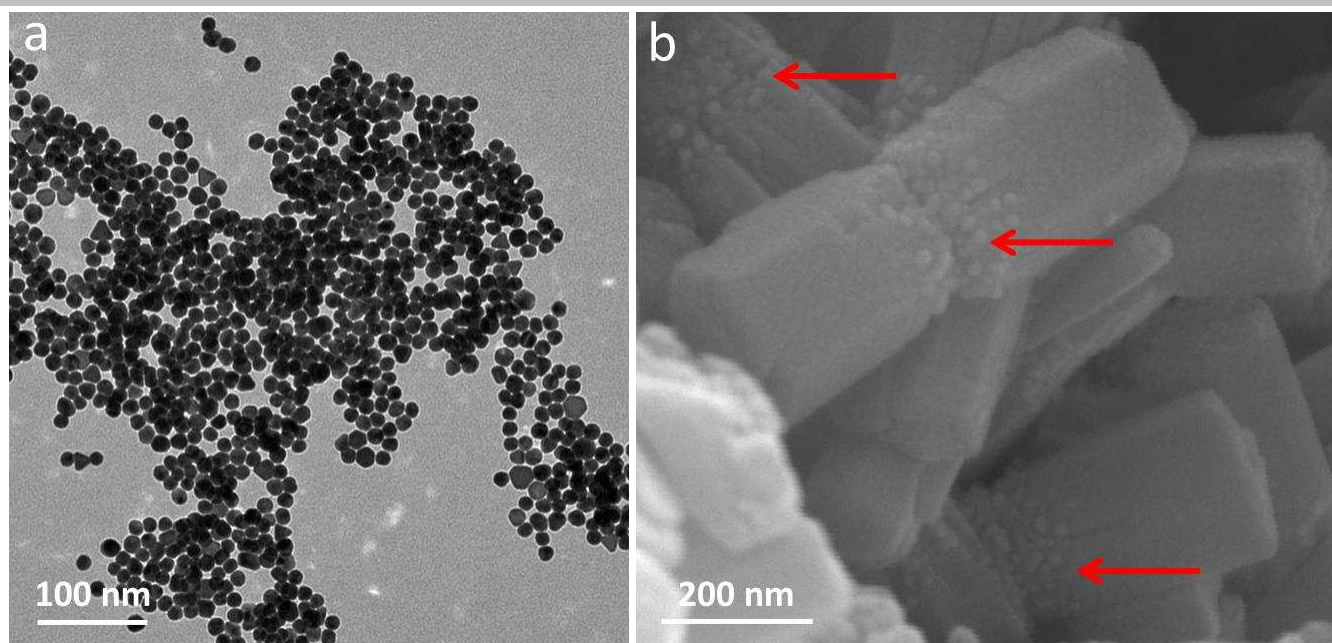


**Figure S5.** Occlusion of 14 nm  $G_{70}$ -AuNPs within ZnO crystals. (a) TEM image recorded for 14 nm  $G_{70}$ -AuNPs. (b) SEM image recorded for  $G_{70}$ -Au/ZnO nanocomposite crystals prepared using these 14 nm  $G_{70}$ -AuNPs. The gold nanoparticles localized in the central region of the rod-like ZnO crystals can be clearly identified, as indicated by the red arrows.

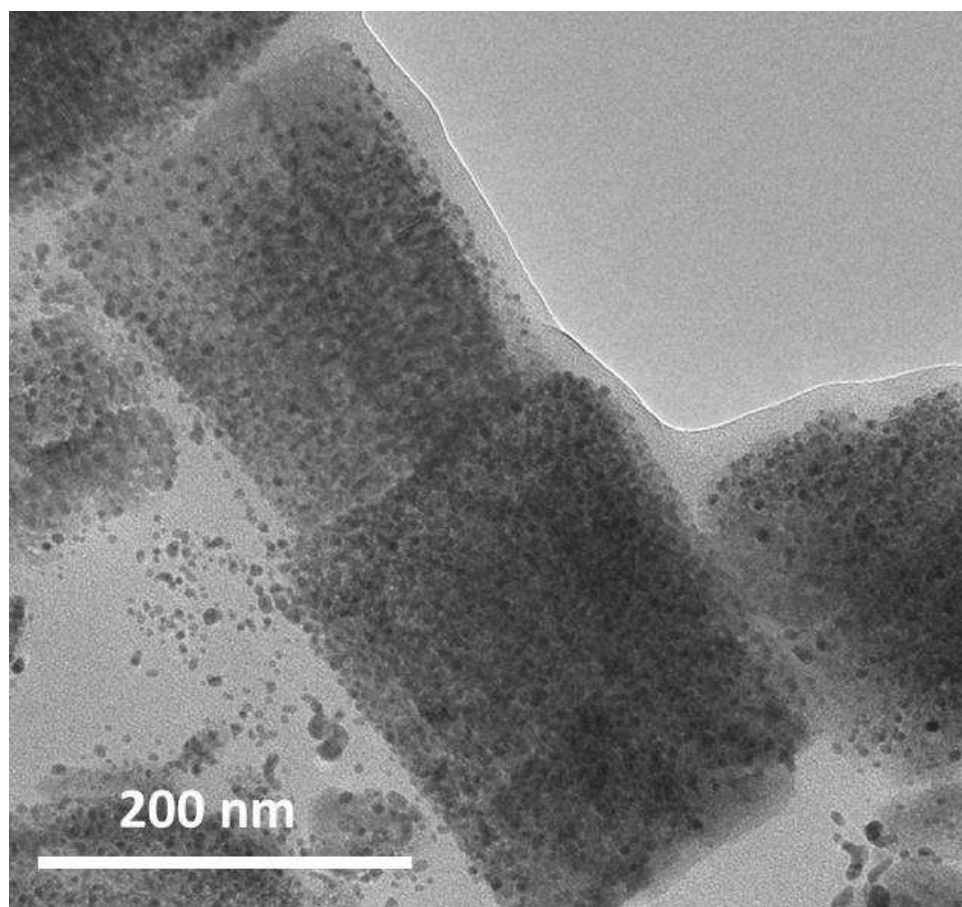


**Figure S6.** TEM image recorded for ultramicrotomed cross-section of G<sub>70</sub>-Au/ZnO nanocomposites prepared in the presence of 0.075 g dm<sup>-3</sup> G<sub>70</sub>-AuNPs.

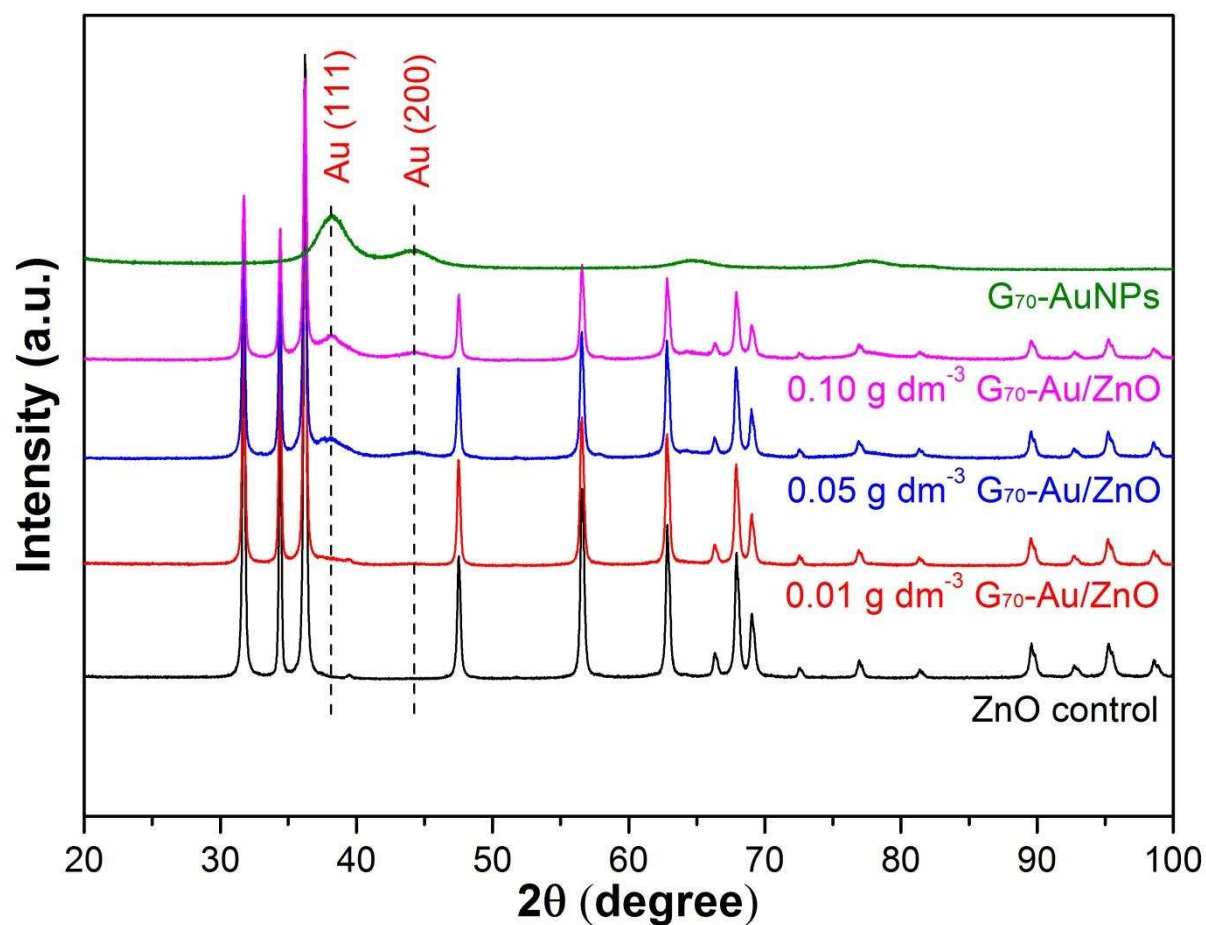


**Figure S7.** Powder X-ray diffractograms recorded for three examples of  $G_{70}$ -Au/ZnO crystals prepared using the stated  $G_{70}$ -AuNP concentrations, plus the  $G_{70}$ -AuNPs alone and a ZnO control.

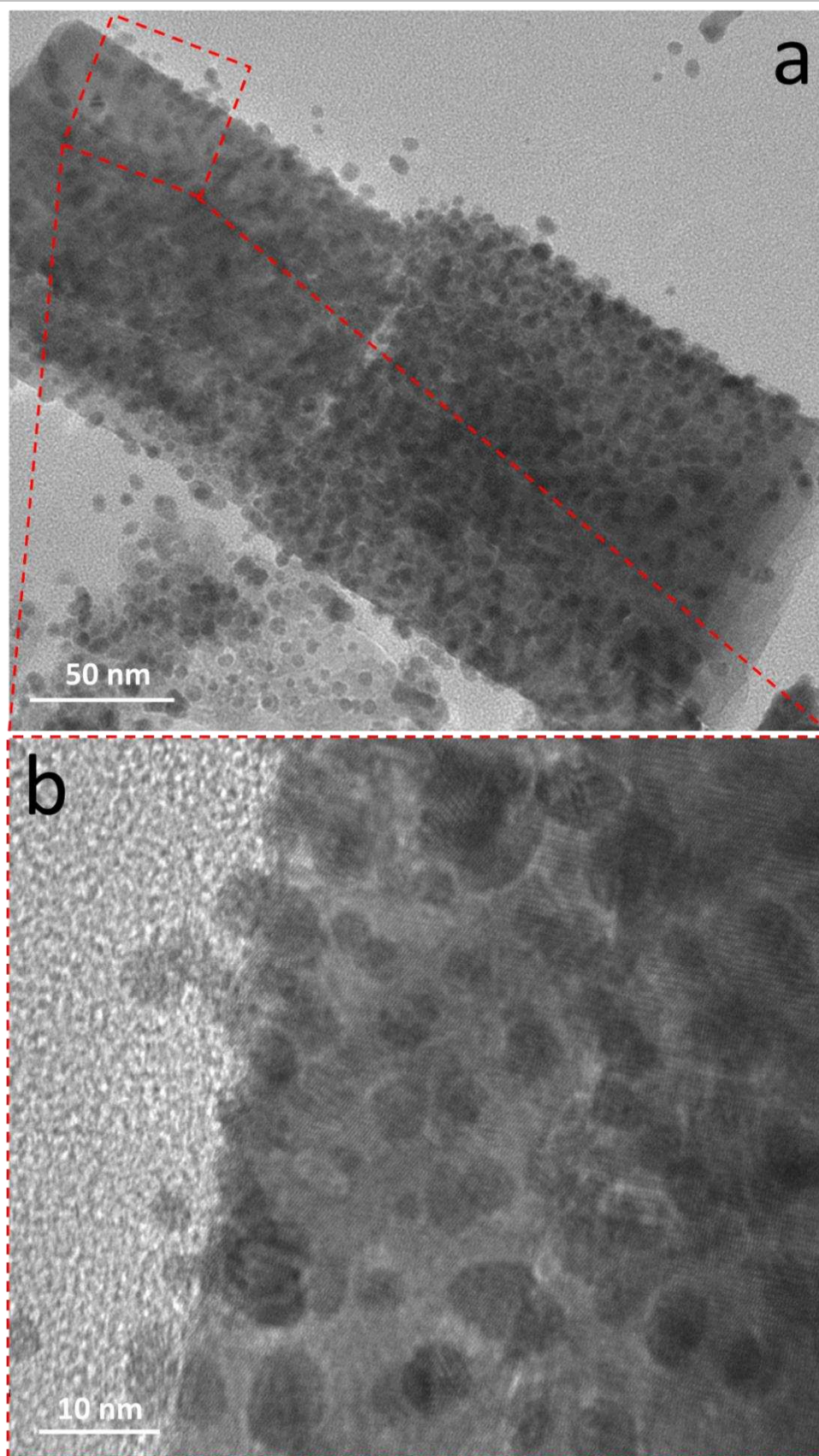


**Figure S8.** (a) High resolution TEM images of cross-section paralleled to the *c*-axis. (b) The corresponding magnified area indicated in (a).

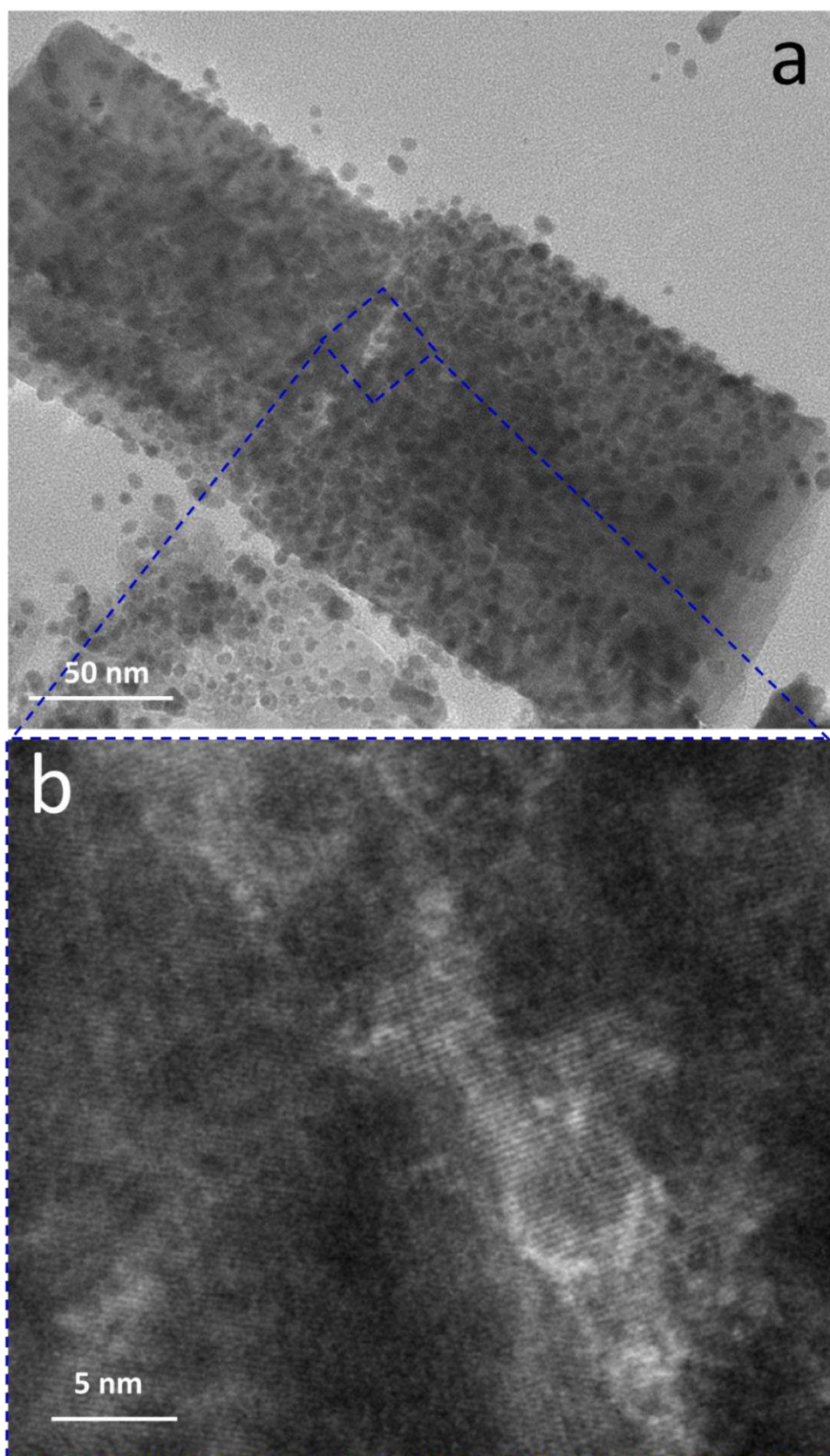


**Figure S9.** (a) High resolution TEM images of cross-section paralleled to the *c*-axis. (b) The corresponding magnified area indicated in (a).

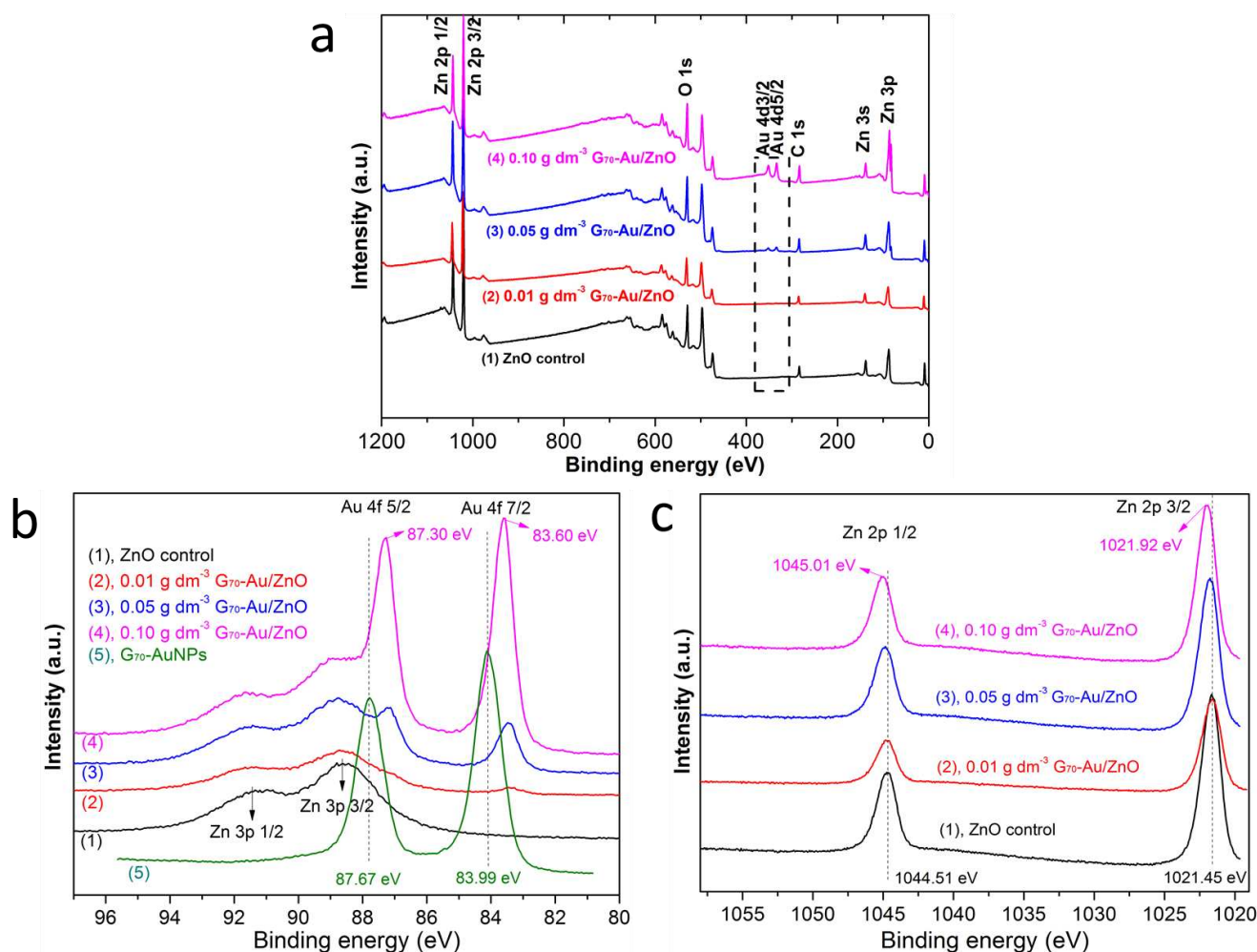


**Figure S10.** (a) XPS spectra recorded for  $G_{70}$ -Au/ZnO nanocomposites prepared at the three stated  $G_{70}$ -AuNP concentrations. The Au4d signal intensity systematically increased when using higher  $G_{70}$ -AuNP concentrations, as indicated by the black dotted lines. High resolution X-ray photoelectron spectra recorded for various  $G_{70}$ -Au/ZnO nanocomposite crystals and appropriate reference materials: (b) Au4f; (c) Zn2p.

The signal intensity of two binding energy (BE) peaks corresponding to the electronic states of Au4f5/2 (87.30 eV) and Au 4f7/2 (83.60 eV) was systematically enhanced at higher AuNP contents. Importantly, each signal was shifted to a lower BE for the  $G_{70}$ -Au/ZnO nanocomposite crystals, whereas the two Zn2p signals were shifted to higher BE. These observations suggest significant charge transfer between the two components, indicating an intimate interaction between the AuNPs and the ZnO host crystal.<sup>[8]</sup>

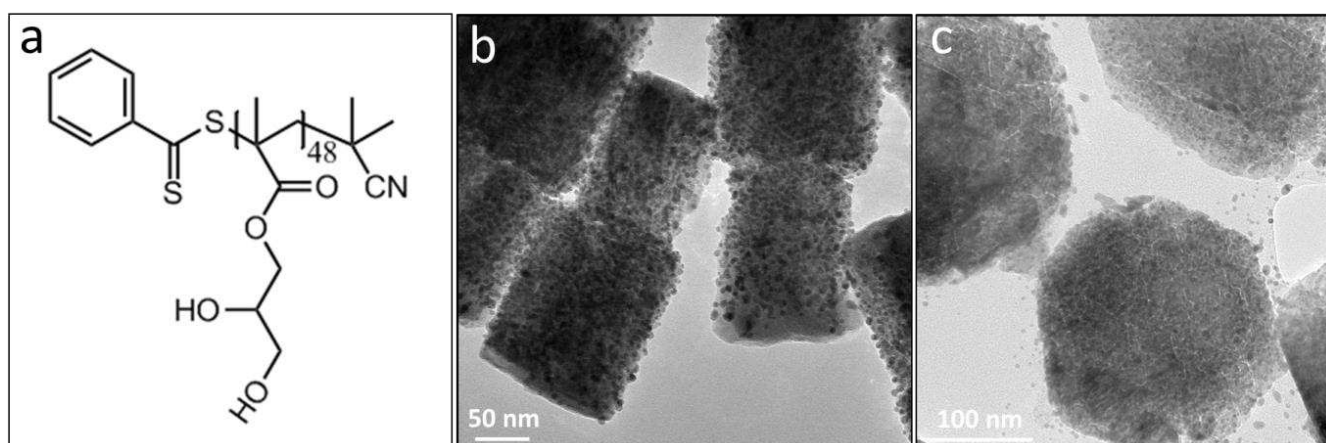


**Figure S11.** Occlusion of  $G_{48}$ -AuNPs (prepared using a poly(glycerol monomethacrylate) $_{48}$  ( $G_{48}$ ) stabilizer containing no carboxylic acid end-groups) within ZnO crystals. (a) Chemical structure of the  $G_{48}$  polymeric stabilizer; (b) TEM image of the as-synthesized  $G_{48}$ -Au/ZnO nanocomposite crystal; (c) cross-sectional TEM image obtained for  $G_{48}$ -Au/ZnO nanocomposite crystals after ultramicrotomy perpendicular to the  $c$  axis. Clearly,  $G_{48}$ -AuNPs are uniformly distributed throughout the whole ZnO crystal. For these experiments,  $G_{48}$  was prepared via reversible addition-fragmentation chain transfer (RAFT) polymerization in ethanol using 2-cyano-2-propyl benzodithioate (CPB) and 2,2'-azobis(isobutylnitrile) (AIBN) as the RAFT chain transfer agent and initiator, respectively. This synthetic protocol produces  $G_{48}$  stabilizer chains with no terminal carboxylic acid unit, which demonstrates that such end-groups are not required for efficient occlusion of  $G_{48}$ -AuNPs within ZnO crystals.

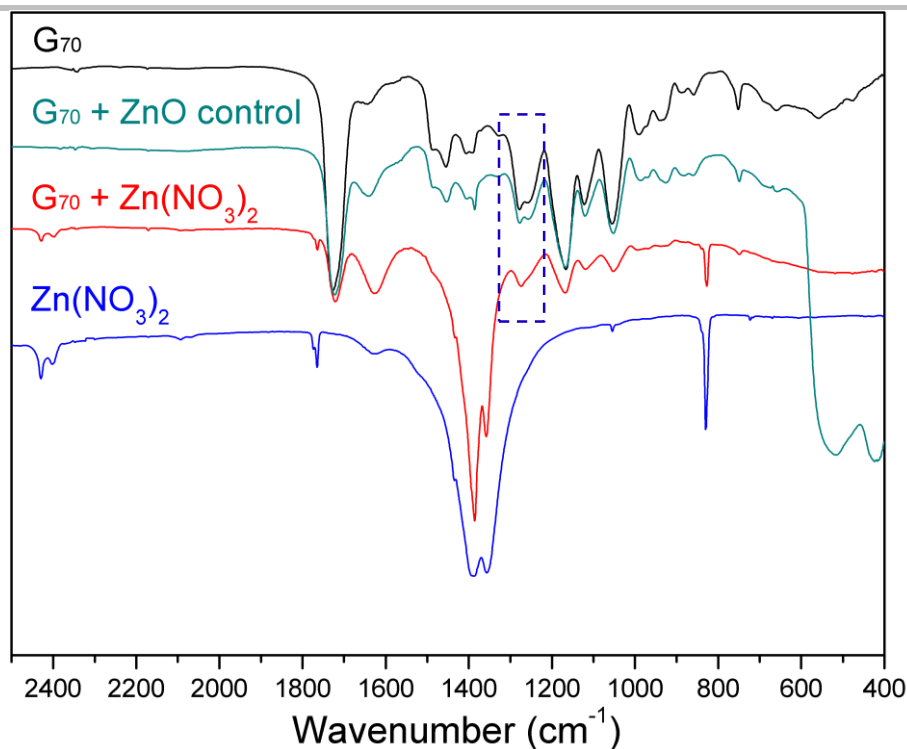


**Figure S12.** Transmission mode FT-IR spectra recorded for G<sub>70</sub>, an ad-mixture of G<sub>70</sub> plus ZnO, an ad-mixture of G<sub>70</sub> plus Zn(NO<sub>3</sub>)<sub>2</sub> (prepared by freeze-drying a binary aqueous solution overnight), and Zn(NO<sub>3</sub>)<sub>2</sub> alone. Clearly, the G<sub>70</sub> plus Zn(NO<sub>3</sub>)<sub>2</sub> spectrum is a combination of the G<sub>70</sub> and Zn(NO<sub>3</sub>)<sub>2</sub> reference spectra, except that the two in-plane bending  $\delta_{\text{C-OH}}$  vibrations merge into a single band, as indicated by the dotted blue box. This strongly suggests chelation between Zn<sup>2+</sup> ions and the cis-diol groups on the G<sub>70</sub> stabilizer chains, for which there is good literature precedent (see ref. 17 in the main manuscript). Notably, for the G<sub>70</sub> plus ZnO control, the  $\delta_{\text{C-OH}}$  in-plane bending vibrations remain as two distinct bands, confirming that no interaction occurs on simple physical mixing of these two components.

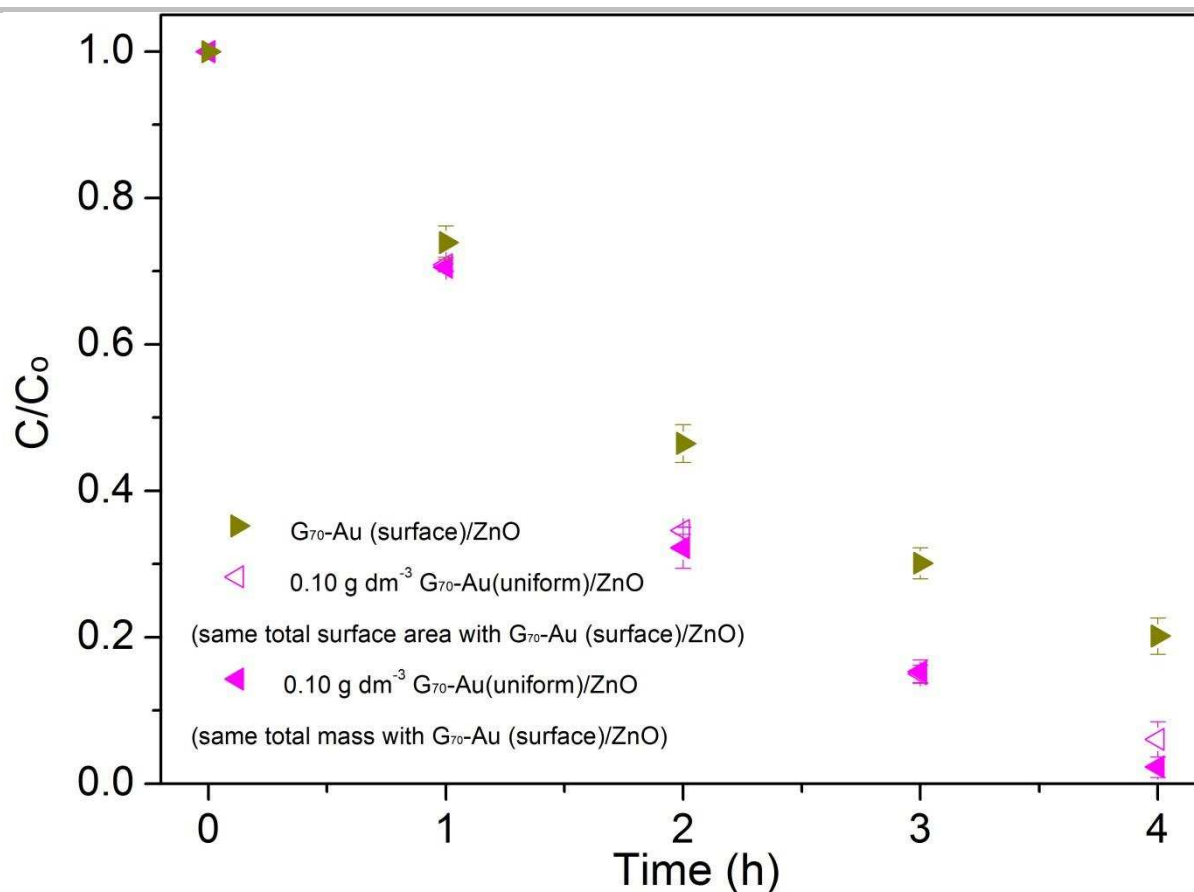


**Figure S13.** Relative rates of UV-induced photocatalytic decomposition observed for a rhodamine B (RhB) dye in the presence of G<sub>70</sub>-Au(surface)/ZnO and 0.10 g dm<sup>-3</sup> G<sub>70</sub>-Au(uniform)/ZnO. The amount of 0.10 g dm<sup>-3</sup> G<sub>70</sub>-Au(uniform)/ZnO crystals used in these experiments was reduced to produce approximately the same total surface area as that for the G<sub>70</sub>-Au (surface)/ZnO crystals, but this had almost no discernible effect on the rate of dye decomposition.

It is well-known that Au/ZnO nanostructures can exhibit superior photocatalytic performance compared to ZnO alone.<sup>[9]</sup> Given that such dye decomposition involves heterogeneous catalysis, the total available surface area could potentially affect photocatalytic performance. However, a control experiment conducted at constant surface area revealed little or no change in the rate of dye decomposition (**Figure S13**). Meanwhile, 0.05 g dm<sup>-3</sup> G<sub>70</sub>-Au(central)/ZnO also exhibits a higher catalytic efficiency compared to G<sub>70</sub>-Au(surface)/ZnO (8.0% vs. 20% dye remains after 4 h). As shown in **Table S1**, 0.05 g dm<sup>-3</sup> G<sub>70</sub>-Au(central)/ZnO has approximately twice the Au content compared to G<sub>70</sub>-Au(surface)/ZnO, but the Au<sub>4d</sub>/Zn<sub>2p</sub> surface atomic ratio for the former is around half that of the latter. This observation

indicates that the photocatalytic performance mainly depends on the bulk Au content, rather than the surface Au content. In other words, the incorporated AuNPs contribute significantly to the rate of photocatalysis. This suggests that a higher extent of AuNP occlusion within ZnO provides a larger number of electron ‘sinks’, which facilitate charge carrier separation and extend the lifetime of the electron-hole pair,<sup>[9a, 10]</sup> thus producing a more effective photocatalyst.

**Table S1. Summary of Au4d/Zn2p atomic ratio (%), solid-state density, BET specific surface area, extent of occlusion of G<sub>70</sub>-AuNPs within ZnO crystals, and pseudo-first-order rate constant for the UV photodegradation of a model dye (rhodamine B).**

Sample	Au4d/Zn2p atomic ratio (%)	Density (g cm <sup>-3</sup> ) <sup>a</sup>	BET surface area (m <sup>2</sup> g <sup>-1</sup> )	Extent of occlusion (% w/w)				Rate constant (k, h <sup>-1</sup> ) <sup>b</sup>
				ICP-MS		Helium pycnometry		
				Au	G <sub>70</sub> -Au	Au	G <sub>70</sub> -Au	
ZnO control	0	5.45	4.2 ± 0.2	-	-	-	-	0.18
0.01 g dm <sup>-3</sup> G <sub>70</sub> -Au/ZnO	0.9	5.41	3.8 ± 0.3	1.3	2.2	1.1	1.9	0.27
0.05 g dm <sup>-3</sup> G <sub>70</sub> -Au/ZnO	7.4	5.22	7.3 ± 0.2	7.0	11.6	6.4	10.7	0.63
0.10 g dm <sup>-3</sup> G <sub>70</sub> -Au/ZnO	39.0	5.05	8.4 ± 0.1	11.9	19.9	11.5	19.1	0.84
G <sub>70</sub> -Au (surface)ZnO	15.0	5.31	3.1 ± 0.4	3.4	5.7	3.9	6.4	0.42

<sup>a</sup> G<sub>70</sub>-AuNPs have a density of 3.85 g cm<sup>-3</sup>, therefore the higher the G<sub>70</sub>-Au content, the lower the density of the nanocomposite crystals.

<sup>b</sup> Pseudo-first-order rate constant (k) is derived from  $-\ln(C/C_0) = kt$

For helium pycnometry, given the solid-state densities of the ZnO control (5.45 g cm<sup>-3</sup>) and the G<sub>70</sub>-AuNPs (3.85 g cm<sup>-3</sup>), the G<sub>70</sub>-AuNP content of these nanocomposite crystals can be determined by measuring their solid-state density via helium pycnometry. These density data are in fairly good agreement with the ICP-MS results.

---

**References**

- [1] G. Frens, *Nature* **1973**, 241, 20-22.
- [2] Z. L. Wang, *J. Phys. Condens. Matter.* **2004**, 16, R829-R858.
- [3] a) S. Cho, H. Jeong, D.-H. Park, S.-H. Jung, H.-J. Kim, K.-H. Lee, *CrystEngComm* **2010**, 12, 968-976; b) Q. Yu, C. Yu, H. Yang, W. Fu, L. Chang, J. Xu, R. Wei, H. Li, H. Zhu, M. Li, G. Zou, G. Wang, C. Shao, Y. Liu, *Inorg. Chem.* **2007**, 46, 6204-6210.
- [4] H. Tada, *J. Am. Chem. Soc.* **1960**, 82, 255-263.
- [5] J. W. Hotchkiss, A. B. Lowe, S. G. Boyes, *Chem. Mater.* **2007**, 19, 6-13.
- [6] a) G. Schneider, G. Decher, *Nano Lett.* **2004**, 4, 1833-1839; b) Y. Jiang, S. Huo, T. Mizuhara, R. Das, Y.-W. Lee, S. Hou, D. F. Moyano, B. Duncan, X.-J. Liang, V. M. Rotello, *ACS nano* **2015**, 9, 9986-9993.
- [7] B. F. Akpınar, Lee; Cunningham, Victoria; Ning, Yin; Mykhaylyk, Oleksandr; Fowler, Patrick; Armes, Steven, *Macromolecules* **2016**, 49, 5160–5171.
- [8] A. E. DiCorato, E. Asenath-Smith, A. N. Kulak, F. C. Meldrum, L. A. Estroff, *Cryst. Growth & Des.* **2016**, 16, 6804-6811.
- [9] a) H. Cui, Z. Chen, S. Zhong, K. L. Wooley, D. J. Pochan, *Science* **2007**, 317, 647-650; b) P. Li, Z. Wei, T. Wu, Q. Peng, Y. Li, *J. Am. Chem. Soc.* **2011**, 133, 5660-5663; c) Y. Chen, D. Zeng, K. Zhang, A. Lu, L. Wang, D.-L. Peng, *Nanoscale* **2014**, 6, 874-881.
- [10] S. T. Kochuveedu, Y. H. Jang, D. H. Kim, *Chem. Soc. Rev.* **2013**, 42, 8467-8493.